

pubs.acs.org/JACS Article

Band Gap Narrowing in a High-Entropy Spinel Oxide Semiconductor for Enhanced Oxygen Evolution Catalysis

Rowan R. Katzbaer, Francisco Marques dos Santos Vieira, Ismaila Dabo,* Zhiqiang Mao,* and Raymond E. Schaak*



Cite This: J. Am. Chem. Soc. 2023, 145, 6753-6761



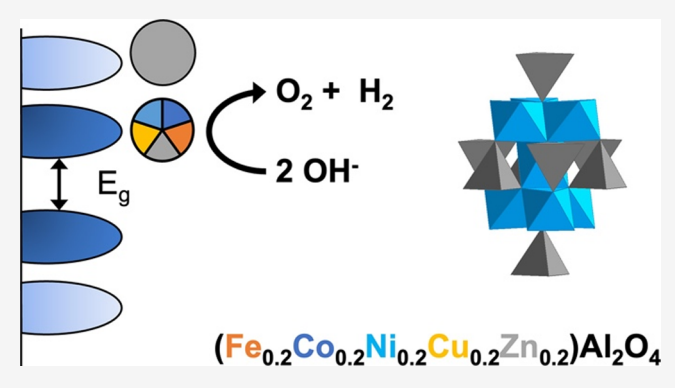
ACCESS I

III Metrics & More

Article Recommendations

s Supporting Information

ABSTRACT: High-entropy oxides (HEOs), which contain five or more metal cations that are generally thought to be randomly mixed in a crystalline oxide lattice, can exhibit unique and enhanced properties, including improved catalytic performance, due to synergistic effects. Here, we show that band gap narrowing emerges in a high-entropy aluminate spinel oxide, (Fe_{0.2}Co_{0.2}Ni_{0.2}Cu_{0.2}Zn_{0.2})Al₂O₄ (A⁵Al₂O₄). The 0.9 eV band gap of A⁵Al₂O₄ is narrower than the band gaps of all parent spinel oxides. First-principles calculations for multicomponent AAl₂O₄ spinels indicate that the band gap narrowing arises from the broadening of the energy distribution of the 3d states due to variations in the electronegativities and crystal field splitting across the 3d transition-metal series. As a catalyst for the oxygen



evolution reaction in an alkaline electrolyte, $A^5Al_2O_4$ reaches a current density of 10 mA/cm² at an overpotential of 400 mV, outperforming all of the single-metal end members at an applied potential of 1.7 V vs RHE. Catalyst deactivation occurs after 5 h at 10 mA/cm² and is attributed, based on elemental analysis and grazing-incidence X-ray diffraction, to the formation of a passivating layer that blocks the high-entropy oxide surface. This result helps to validate that the HEO is the active catalyst. The observation of band gap narrowing in $A^5Al_2O_4$ expands the scope of synergistic properties exhibited by high-entropy materials and offers insight into the question of how the electronic structure of multicomponent oxide materials can be engineered via a high-entropy approach to achieve enhanced catalytic properties.

■ INTRODUCTION

High-entropy materials, which are alloys that have a random distribution of five or more atoms within certain lattice sites, form because the configurational entropy associated with the mixing of the elements overcomes the propensity for enthalpically favorable phase segregation. The random mixing of elements also leads to unique physical properties, such as extremely high durability, magnetic frustration, or surface sites with unique electronic structures that can enable high catalytic activity. 1-5 High-entropy oxides (HEOs) are a subclass of these materials, with the rock-salt structure oxides, such as (Co_{0.2}Cu_{0.2}Mg_{0.2}Ni_{0.2}Zn_{0.2})O, being among the most studied, as they have potential applications as dielectrics and as capacitors.3 High-entropy perovskites and spinels have also been investigated, primarily for applications as catalyst supports or as magnets. 1,6 Based on these and other examples, it is clear that the properties of high-entropy materials, including oxides, are not necessarily a linear combination of those of their end members. For example, $Mg_{0.167}N_{0.167}Cu_{0.167}Co_{0.167}Zn_{0.167}Ge_{0.167}O\ \ has\ \ a\ \ low\ \ thermal$ conductivity that is more similar to that of an amorphous material than any of the constituent single-metal oxides while

maintaining mechanical stiffness.⁴ A considerable improvement in performance is also seen when using NiMgCuZnCoO_x as a support for Pt-catalyzed CO oxidation.⁷

The electronic properties of high-entropy materials are especially intriguing. Recently, it was discovered that, in the high-entropy alloy RuRhPdAgOsIrPtAu, metals lose their individual electronic character and overall electronic degeneracy is lowered. Understanding the electronic structure of HEOs, with more isolated metal sites than in alloys and a wider range of structures, is still in the nascent stages. In the rare earth oxide (CeGdLaNdPrSmY)O $_{2-\delta}$, the band gap of 2.11 eV is smaller than the 3 eV band gap of the CeO $_2$ end member. While the ability of both Ce and Pr to adopt a 4+ oxidation state allows for significant oxygen vacancies, 1 eV is a greater band gap reduction than would be expected from oxygen

Received: December 4, 2022 Published: March 15, 2023





vacancies alone. It is thought that the Pr⁴⁺ oxidation state is essential for allowing the band gap to narrow from 3 to 2.11 eV, in line with the observation that the ternary alloy, (CeLaPr)O_{2- δ}, also exhibits band gap narrowing. Lithium doping into MgNiCoCuZnO_x was found to have a similar effect, lowering the band gap from 1 to 0.6 eV through a charge compensation mechanism, whereby some of the transition metals adopt a 3+ oxidation state.

These studies offer insight into the way in which one element can have a disproportionate effect on the electronic properties of a high-entropy material. However, to truly be able to engineer the band gap of HEOs, a more comprehensive theoretical and experimental understanding is needed. Density functional theory (DFT) has been instrumental to both calculate and understand the electronic band structures of HEOs. However, the substantial supercell size needed to accurately model both the random cation distribution and the resulting crystal structure distortions makes these simulations computationally costly. The local distortion around the cations has been shown to change the degeneracy and ground state of the metals, so accurate modeling is essential to gain a theoretical understanding of band structures in HEOs.

High-entropy spinel oxides, AB_2O_4 , are of interest for their magnetic and catalytic properties 5,15,16 and are also intriguing platforms for interrogating electronic structure effects. Like other HEO magnets, competing magnetic coupling due to mixed magnetic elements often makes it difficult to predict the magnetic state of the high-entropy phase. 1,17-19 In aluminumbased spinel oxides that contain Al on the B sites and magnetic metal cations on the A sites, the spin state is generally paramagnetic at room temperature.²⁰ The spinel-type AAl_2O_4 compounds (A = Fe, Co, Ni, Cu, or Zn) include as end members the magnetic FeAl2O4, CoAl2O4, and NiAl2O4 materials.²⁰ All end members are also semiconductors, with band gaps ranging from 1.6 eV for FeAl2O4 to 4.2 eV for ZnAl₂O₄. ²¹ We show here that the band gap of the highentropy spinel oxide that contains all five of these metals, (Fe_{0.2}Co_{0.2}Ni_{0.2}Cu_{0.2}Zn_{0.2})Al₂O₄ (which we hereafter refer to as A⁵Al₂O₄), is 0.9 eV, which is smaller than all of the singlemetal spinel oxide end members. This unexpected finding adds to our growing knowledge of the synergistic properties of highentropy materials by demonstrating that the band gap is not a simple average of the end members. DFT band gap calculations reveal that a fundamental shift occurs in the energy levels of the transition metals in the high-entropy spinel oxide. This study demonstrates that the electronic structure of materials can be engineered via high-entropy stabilized structures to achieve enhanced properties. It expands the possibility of band gap narrowing into ternary transition metal oxides, suggesting that the previous studies on oxides containing rare earth metals or alkali metals 11,13 may fit into a larger framework by which to understand the band structures of HEOs.

Band gap narrowing, as observed in $A^5 Al_2 O_4$, can lead to higher electrical conductivity, which can enhance properties such as electrocatalysis that require rapid transport of electrons through the material. High-entropy materials have become prominent targets in catalysis due to advantageous effects such as synergetic active sites and enhanced stability. $^{5,6,16,22-24}$ High-entropy catalysts for the oxygen evolution reaction (OER), which is a bottleneck reaction in overall water splitting and is a key component of air—water batteries, 25 have shown improvements in both the rate of catalysis and durability. 5,16,22

Oxides containing the transition metals manganese, cobalt, and iron^{26,27} are well known as OER catalysts in alkaline electrolytes, which are applicable to alkaline fuels cells and water electrolyzers that are both considered key technologies for decarbonization.²⁵ Al has also been shown to synergistically improve the performance of Co-Ni alloys as OER catalysts. 28,29 Accordingly, in addition to demonstrating band gap narrowing, we show that the high-entropy A⁵Al₂O₄ spinel has enhanced catalytic activity, relative to the AAl₂O₄ end members, for the OER in alkaline electrolytes, which can be attributed, in part, to its narrowed band gap and electronic structure. By examining the surface of the material beyond the limits of its stability as an OER catalyst, we find evidence for the formation of a passivating layer, as well as evidence for a lack of significant dissolution. These results suggest that the high-entropy phase is indeed the active catalyst since the formation of the passivating layer (which blocks the highentropy phase) deactivates the catalyst. These insights into the origins of band gap narrowing in oxide spinels and their applicability as OER electrocatalysts provide guidelines for designing high-entropy materials with targeted and enhanced properties.

EXPERIMENTAL SECTION

Materials. The following metal salts were obtained from Sigma-Aldrich: Fe(NO₃)₂·9H₂O (>99.95% purity), Co(NO₃)₂·6H₂O (99.999% purity), Ni(NO₃)₂·6H₂O (99.999% purity), Cu(NO₃)₂·3H₂O (99–104% purity), Zn(NO₃)₂·6H₂O (>99% purity), and Al(NO₃)₃·9H₂O (99.997% purity). KOH (85% purity) was obtained as pellets from VWR. Isopropyl alcohol (99.7% purity) was obtained from VWR. Nafion perfluorinated resin, 5 wt % in lower aliphatic alcohols and water, was obtained from Sigma-Aldrich. IrO₂ (99.0% purity) was obtained from Sigma-Aldrich.

Synthesis. The synthesis of all materials was achieved through a solution combustion method adapted from Han et al.²¹ The relevant metal nitrate hydrates [Fe(NO₃)₂·9H₂O, Co(NO₃)₂·6H₂O, Ni- $(NO_3)_2 \cdot 6H_2O$, $Cu(NO_3)_2 \cdot 3H_2O$, and/or $Zn(NO_3)_2 \cdot 6H_2O$], aluminum nitrite nonahydrate, and glycine, in a ratio of 1 mmol:2 mmol:2 mmol, were dissolved in 15 mL of Nanopure distilled deionized (DI) water. For the end members FeAl₂O₄, CoAl₂O₄, NiAl₂O₄, CuAl₂O₄, and ZnAl2O4, the masses of the appropriate metal nitrate hydrates were 404.00, 291.03, 290.80, 241.60, and 297.49 mg, respectively. For the high-entropy A⁵Al₂O₄ spinel, the masses of each of the metal nitrate hydrates were 80.80, 58.21, 58.16, 48.32, and 59.50 mg, respectively. The transition metal nitrates in the high-entropy A⁵Al₂O₄ spinel were equal to 1 mmol in total, with each metal present at 0.2 mmol. For (Co,Ni)Al₂O₄, 145.52 mg of Co(NO₃)₂·6H₂O and 145.04 mg of Ni(NO₃)₂·6H₂O were used. For all reactions, 2 mmol each of aluminum nitrite nonahydrate (750.26 mg) and glycine (150.14 mg) were used. After dissolution, the solution was placed in a 50 mL alumina crucible. The crucible was fired in a large Carbolyte box furnace preheated to 400 °C. The reaction was held for 1 h to allow for complete combustion. Each compound was then annealed at 1100 °C for 8 h, after which the furnace was allowed to cool to room temperature.

X-ray Diffraction. Powder X-ray diffraction (PXRD) data were obtained on a Malvern Panalytical Empyrean diffractometer. The instrument was equipped with a copper source, operated at a voltage of 45 keV and a power of 40 kW. PXRD patterns were obtained utilizing reflection mode and a PIXcel 3D detector. Grazing-incidence XRD (GIXRD) data were obtained on a Malvern Panalytical Empyrean diffractometer, operated similarly to PXRD data collection. The instrument was operated with a low (10°) fixed incident angle to maximize signal obtained from the surface of the material.

Scanning Electron Microscopy. Scanning electron microscopy with energy-dispersive X-ray spectroscopy (SEM-EDX) was utilized to determine the elemental composition and distribution of elements

in the bulk powders. Data were collected on an ESEM Q250 with a tungsten source. The instrument was operated at 7 keV under ultrahigh vacuum. Imaging and mapping of elemental composition were done utilizing secondary electrons. For elemental mapping, an EDS Bruker AXS detector was used. Elemental maps were constructed using the Aztec software, which performed automatic peak integrations of the spectra to determine elemental composition, as well as allowing visualization of the location of elements.

Elemental Analysis. To further investigate the elemental composition of the high-entropy $A^5 {\rm Al_2O_4}$ spinel and to monitor possible elemental leaching during electrochemical testing, inductively coupled plasma mass spectrometry (ICP-MS) was performed on a Thermo Scientific iCAP TQe Quadrupole ICP-MS instrument. For analysis of the high-entropy $A^5 {\rm Al_2O_4}$ spinel, approximately 10 mg of material was dissolved in hydrofluoric acid. The sample was then diluted to a parts-per-million concentration. For analysis of the electrolyte during electrochemical stability testing, an aliquot was taken and added to a 5% by volume nitric acid solution. Due to the high environmental levels of iron and aluminum that can often inhibit accuracy, great care was taken to only use metal-free plastic for the transfer and storage of the solutions.

Diffuse Reflectance Spectroscopy. Diffuse reflectance spectra were obtained on a Perkin Elmer Lambda 950 UV—visible spectrometer equipped with a 150 mm integrating sphere in diffuse reflection mode. Spectra were collected from 250 to 2500 nm, with 2 nm steps. The reference spectrum for total reflectance was measured against a Spectralon disc standard. To generate samples, the powders were suspended in 1 mL of ethanol by sonication for 10 min. The solution was drop-cast on quartz glass slides (Electron Microscopy Sciences) until opaque. The slides were dried with nitrogen before the measurement. Plots of the Kubelka—Munk function, raised to the power of 2 (direct band gap) vs energy in eV, were constructed. Band gaps were calculated by fitting the linear region in the onset of absorption and extrapolating to the *x*-intercept. 30,31

X-ray Photoelectron Spectroscopy. X-ray photoelectron spectroscopy (XPS) data were collected using a Physical Electronics VersaProbe II instrument equipped with a monochromatic Al $K\alpha$ X-ray source ($h\nu$ = 1486.7 eV) and a concentric hemispherical analyzer. Charge neutralization was performed using both low energy electrons (<5 eV) and argon ions. The binding energy axis was calibrated using sputter cleaned Cu (Cu $2p_{3/2} = 932.62$ eV, Cu $3p_{3/2} = 75.1$ eV) and Au (Au $4f_{7/2} = 83.96$ eV) foils. Given the low carbon signal and interferences, peaks were charge referenced to Al in the 2p spectra at 74.4 eV. Measurements were made at a takeoff angle of 45° with respect to the sample surface plane. This resulted in a typical sampling depth of 3–6 nm (95% of the signal originated from this depth or shallower).

Electrocatalysis. All electrochemical experiments were conducted in 1 M KOH utilizing a rotating disk working electrode, a graphite rod counter electrode, and a mercury-mercury oxide reference electrode, which is a stable reference in base. The working electrode substrate was glassy carbon, polished to 1/4 micron smoothness by utilizing diamond paste on a polishing cloth. Polishing was conducted at 9 microns, 3 microns, 1 micron, 1/2 micron, and 1/4 micron to ensure a smooth and clean surface. The electrode ink was made by sonicating 2 mg of the catalyst powder, 20 μ L of Nafion perfluorinated resin in a solvent mixture of 400 μ L of Nanopure water and 100 μ L of isopropyl alcohol. Sonication was conducted for 1 h. Then, 20 µL of the catalyst ink was deposited on the glassy carbon electrode to maintain consistent catalyst loading and to ensure good contact between the electrode and catalyst. For $\text{IrO}_{2^{\prime}}$ the powder was pressed into a pellet and sintered for 2 h at 800 °C to obtain a surface area comparable to the spinel oxides; the pellet was then ground before creating the catalyst ink. Potentials were applied utilizing a Gamry 1000b potentiostat.

Electrical Measurements. Measurements were conducted on pellets pressed at 50 MPa in a hydrolytic press and then sintered for 1 h at 1100 °C. Silver electrodes (5 mm diameter, 100 nm thick) were sputtered on the samples. Electrochemical impedance spectra were

then obtained using a Modulab XM MTS system at frequencies ranging from $0.01~\mathrm{Hz}$ to $100~\mathrm{kHz}.$

Electronic-Structure Predictions. First-principles calculations were performed using the plane-wave (PW) pseudopotential method implemented in the Quantum-ESPRESSO suite $^{32-34}$ with the Perdew-Burke-Ernzerhof (PBE)³⁵ parameterization of the generalized gradient approximation and with pseudopotentials from the standard solid-state pseudopotential (SSSP) library. 36,37 Calculations were performed at the GGA + U^{38-40} level using Löwdinorthogonalized atomic projectors 41 with the Hubbard U correction being applied to Fe, Co, Ni, and oxygen when bonded to Ni or Zn. These parameters were obtained by fitting the experimental band gaps of the end-member spinels. The values obtained were $U_{\rm Fe}$ = 8 eV, $U_{\rm Co}$ = 3 eV, $U_{\rm Ni}$ = 8 eV, $U_{\rm O,Ni}$ = 4 eV, and $U_{\rm O,Zn}$ = 5 eV. For all calculations, a 56-atom supercell was employed. The kinetic energy cutoffs for the wavefunctions and charge density were 90 Ry and 1080 Ry, respectively. Geometry optimizations were performed while sampling the Brillouin zone with a Γ-centered Monkhorst-Pack grid of $4 \times 4 \times 4$; optimization was performed until the total force was below 0.0002 Ry/Å (0.0025 eV/Å). In subsequent calculations, the Brillouin zone was sampled with a Γ-centered Monkhorst-Pack grid of $8 \times 8 \times 8$.

RESULTS AND DISCUSSION

The $A^5Al_2O_4$ spinel, as well as the AAl_2O_4 end members, were synthesized as bulk powders using a solution combustion method, as described in the Experimental Section. The formation and phase purities of the spinel oxides were primarily determined by PXRD. For all end members, the expected cubic spinel phase was observed by PXRD as the primary product (Figure S1). FeAl₂O₄, CoAl₂O₄, NiAl₂O₄, and ZnAl₂O₄ appeared as pure crystalline phases by PXRD, based on comparison with patterns simulated from literature data, 42-46 while CuAl₂O₄ had a few additional weak reflections that could not be identified. PXRD also confirms that A⁵Al₂O₄ corresponds to a single-phase cubic spinel, with no observable bulk phase segregation. A Rietveld refinement of the PXRD data for A⁵Al₂O₄ with all five elements modeled at 1/5 occupancy, shown in Figure 1, revealed a cubic lattice parameter of a = 8.096(2) Å (Table S1). This value is within the range of literature lattice parameters for the end members: $FeAl_2O_4$, a = 8.1558 Å; $CoAl_2O_4$, a = 8.1000 Å; $NiAl_2O_4$, a =8.0460 Å; CuAl_2O_4 , a = 8.1000 Å; and ZnAl_2O_4 , a = 8.0880

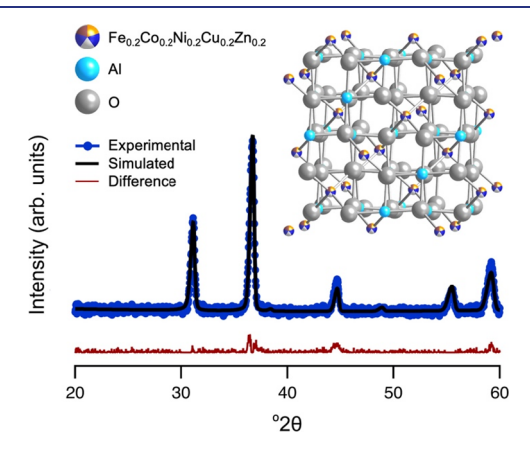


Figure 1. Rietveld refinement for the high-entropy $A^5 Al_2 O_4$ spinel, $(Fe_{0.2}Co_{0.2}Ni_{0.2}Cu_{0.2}Zn_{0.2})Al_2 O_4$. Experimental data are shown in blue circles, the refined pattern is shown as a black trace overlaid on the experimental data, and the difference is shown in red, below the overlaid experimental and simulated patterns. The $A^5 Al_2 O_4$ spinel crystal structure is shown in the inset.

Å. $^{42,44-46}$ Due to the strong preference of Al³⁺ for the octahedral sites in spinels, arising from the lower crystal field energy of Al³⁺ in octahedral vs tetrahedral sites, there is minimal site inversion in aluminate spinels. The has also been observed that Fe²⁺, which generally occupies octahedral sites, favors tetrahedral sites at annealing temperatures over 600 °C. Therefore, the transition metal cations can reasonably be expected to be located in the tetrahedral A sites of the AB_2O_4 compound, while Al³⁺ resides in the octahedral B sites.

ICP-MS (Table S2), which was used to determine the composition of the bulk sample, confirmed that the five transition metals were present in equimolar amounts and that all together, the five transition metals and aluminum were present in a 1:2 ratio to yield a formula of (Fe_{0.2}Co_{0.2}Ni_{0.2}Cu_{0.2}Zn_{0.2})Al₂O₄. To confirm the uniform distribution of metals within the sample, along with their relative atomic percentages, SEM-EDX element mapping was used. As would be expected for a true solid solution, the five transition metals were present across the entire mapped area, along with aluminum and oxygen (Figures 2 and S2). The atomic percentages of the five A-site metals are equal, within typical experimental error for SEM-EDX.

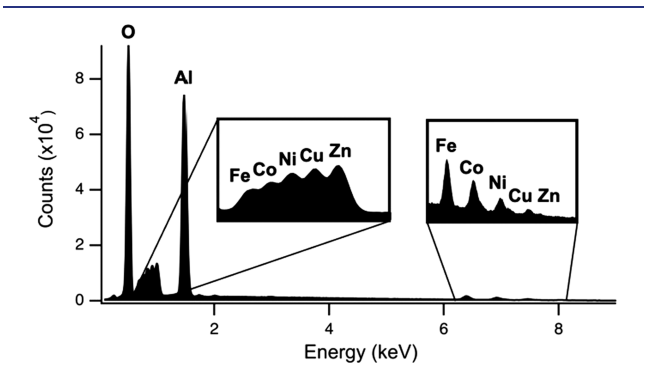


Figure 2. SEM-EDX spectrum showing the presence of Fe, Co, Ni, Cu, and Zn in near-equimolar amounts, as well as the expected 1:2 ratio of the transition metals to Al.

XPS data, shown in Figure 3, confirm the presence of the five metals and aluminum in the surface region of the A⁵Al₂O₄ sample, suggesting that the HEO present in the bulk is also present on the surface. In addition to surface composition, XPS data for A⁵Al₂O₄, along with XPS data for the parent phases and other reference compounds (Figure S3), provide information about the oxidation states of the constituent transition metals. For zinc, the Auger peak was also collected, as calculating the Auger parameter is more indicative of the oxidation state for this element. 48 The Fe 2p_{3/2} peaks for both A⁵Al₂O₄, which is at 711.6 eV, and FeAl₂O₄, which is at 711.45 eV, are consistent with iron in a 2+ oxidation state. 49 However, we cannot rule out the possibility of a more complex oxidation state distribution in A⁵Al₂O₄, since overlap with the cobalt Auger peak prevents unambiguous curve fitting of a pure iron peak. The Co 2p_{3/2} peak of A⁵Al₂O₄ is at 781.9 eV, which is slightly higher in energy than the corresponding peak for CoAl₂O₄, which is at 781.6 eV. Both binding energies are similar to that of CoO, which is at 782.1 eV, and therefore is consistent with cobalt in a 2+ oxidation state. 49 For nickel, the Ni $2p_{3/2}$ binding energy for both $A^5Al_2O_4$ and NiAl₂O₄ falls at 856 eV. Other spinel oxides that contain nickel in the A-site, and that are attributed to Ni2+, have also been reported to be located at 856 or 855.8 eV.49 The Cu 2p_{3/2} binding energy in A⁵Al₂O₄ is 933.3 eV, whereas it is 933.8 eV in CuAl₂O₄. Copper(II) oxide is reported to have the Cu 2p3/2 peak at 933.6 eV,48 providing reasonable confidence that both spinel oxides also contain Cu2+. The Auger parameter for zinc in $ZnAl_2O_4$ was found to be 2009.8 eV, while in $A^5Al_2O_4$, it was calculated to be 2010.6 eV. Both of these values are much closer to the value reported for zinc(II) oxide, at 2010.4 eV, than for zinc metal, which is at 2013.77 eV. 48 Overall, XPS analysis confirms the presence of all metals on the surface and indicates oxidation states of 2+ for all A-site transition metals.

The end members, which are the single-metal AAl_2O_4 spinels, are all semiconductors, with band gaps ranging from ~ 2 to ~ 4 eV (Figure 4a–e), based on diffuse reflectance measurements: FeAl₂O₄ (1.6 eV), CoAl₂O₄ (2.3 eV), NiAl₂O₄ (2.0 eV), CuAl₂O₄ (2.3 eV), and ZnAl₂O₄ (4.2 eV). These band gap values match well with previous reports for these

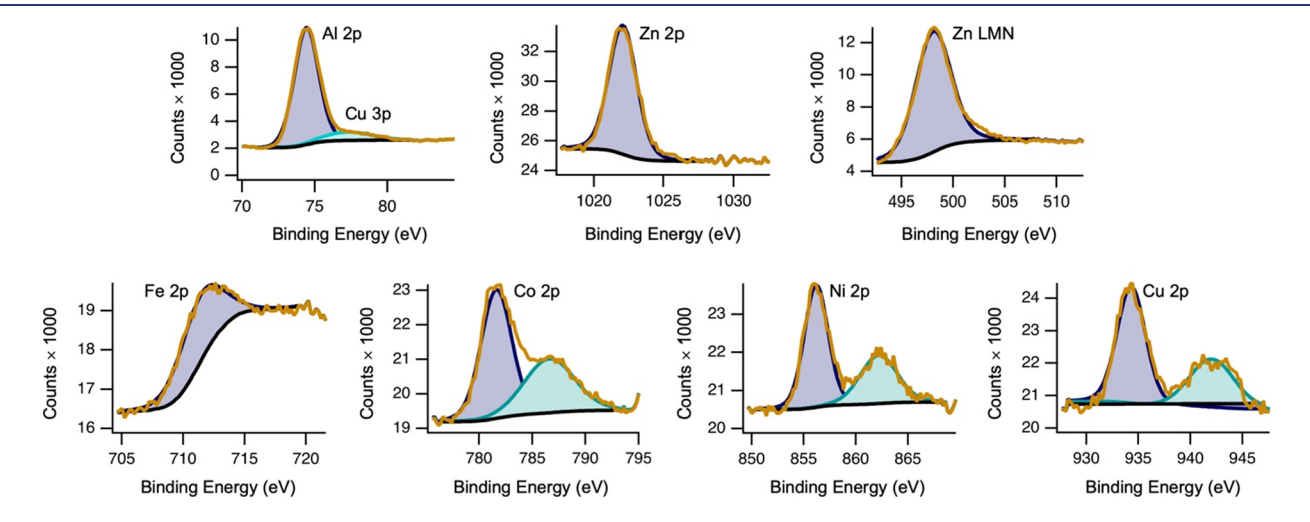


Figure 3. High-resolution XPS spectra (with fitted backgrounds) for the metals that comprise the A^5 Al₂O₄ high-entropy spinel oxide. The Al 2p and Cu 3p peaks overlap, so they are deconvoluted. For Zn, both the Zn 2p and Zn LMN Auger peaks are shown. For Co and Ni, both the main 2p peaks (dark blue) and the 2p plasmonic loss peaks (light blue) are fit. For Cu, both the main 2p peak (dark blue) and the shake-up satellite peak (light blue) are fit.

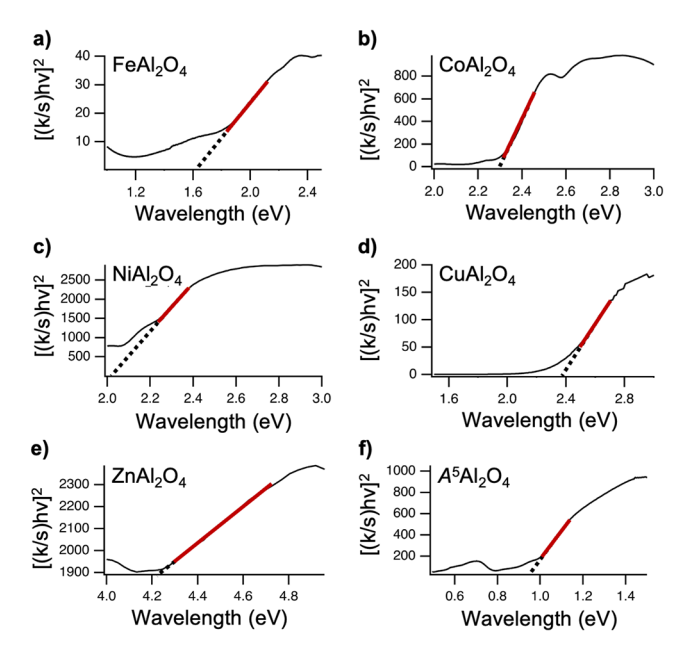


Figure 4. Diffuse reflectance spectra of (a-e) all end member AAl_2O_4 spinels, as well as (f) the high-entropy $A^5Al_2O_4$ spinel. Wavelength is plotted against the Kubelka–Munk function, raised to the power of 2. Band gaps are calculated by extrapolating the linear region to the x-intercept.

phases.²¹ However, in the high-entropy $A^5 Al_2 O_4$ oxide, we observe that the band gap has narrowed to 0.9 eV (Figure 4f), which is lower than the band gaps of all of the end members. This unexpected finding can be understood as resulting from shifted d-band energies. Previous computational work on Fe, Co, or Ni doping of $CuAl_2O_4$ demonstrates that all three of these metals contributed to the density of states just above the Fermi level.⁵⁰ In the high-entropy $A^5Al_2O_4$ spinel, it is expected

that the conduction band will be significantly influenced by the five constituent metals. DFT calculations predict that the binary alloys have a smaller band gap energy than the end members, with a few exceptions that may be an artifact of the specific configurations studied. This is caused by the differing electronegativities, χ , and crystal field splitting, Δ , of the dopant and host transition-metal cations, as shown in Figure 5a. These differences introduce 3d states within the band gap of the host material, as depicted schematically in Figure 5b. Additionally, transition metal dopants having lower Δ can also affect the band gap by reducing the crystal field splitting of the host transition metal; in practice, this lowers the energy of unoccupied t_{2g} states and consequently the band gap energy, as seen in Figure 5c. The intensity of this effect increases with the difference between the crystal field splitting of the host and dopant transition metal. Further, increasing the fraction of the transition metal with lower crystal field splitting causes this effect to be more pronounced. Interestingly, the two mechanisms of band gap reduction can produce two different types of transitions (i.e., bonding-to-antibonding and antibonding-to-antibonding electron transfer) depending on the 3d states from which the band edges originate (Figures S4-S17).

XPS analysis indicated that all five A-site transition metals were present at the surface in the 2+ oxidation state. For the computational studies described above and in Figures 5 and S4–S17, the bulk oxidation states were not constrained and therefore were allowed to vary to minimize the overall energy of the system. As a result of these calculations, the oxidation states could be extracted, along with their distributions, based on their magnetic moments (Figure S5). Consistent with the surface analysis, a 2+ oxidation state was found to be most likely for all five transition metals, suggesting that the bulk oxidation states match those of the surface. The complex interactions in HEOs can support unusual oxidation states for various reasons, as discussed in the Introduction. However,

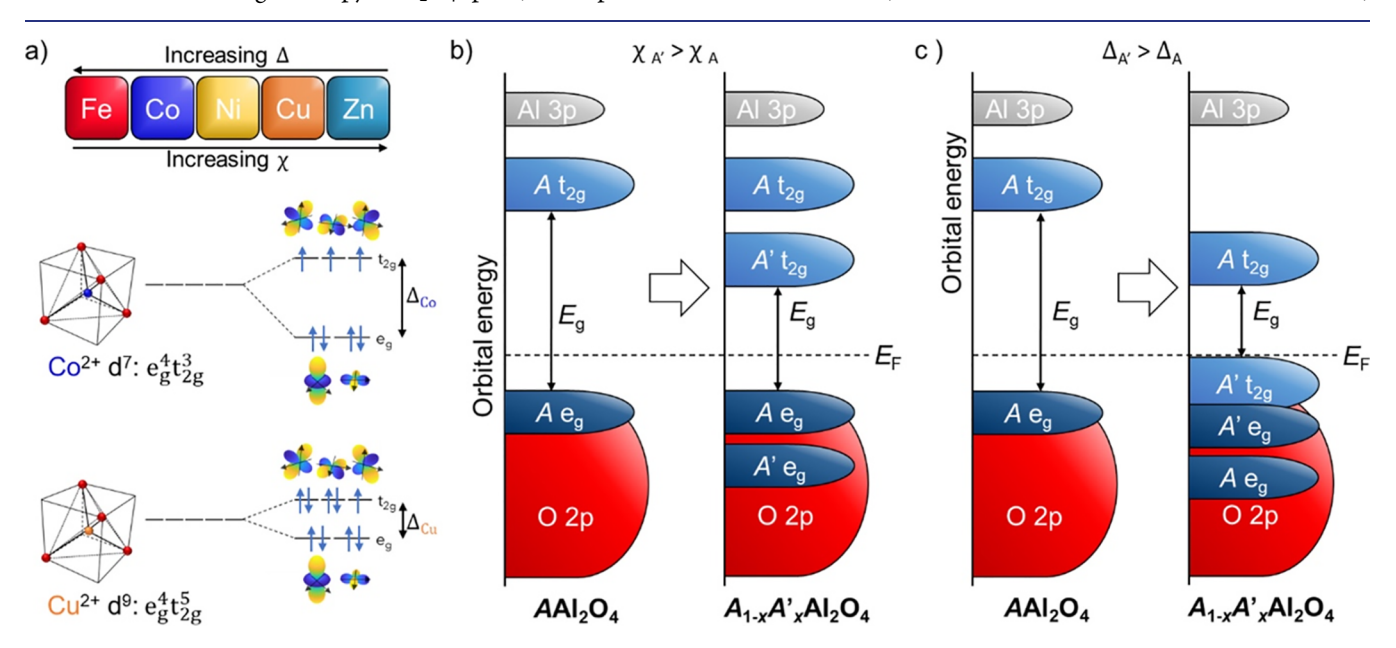


Figure 5. (a) Trends in crystal field splitting Δ and electronegativity χ for the five constituent metals of the high-entropy spinel. Crystal field splitting for tetrahedrally coordinated divalent Co and Cu. (b) The addition of a transition metal of greater electronegativity can reduce the band gap energy by introducing states between the e_g and t_{2g} states of the original transition metal. (c) The addition of a transition metal of lower crystal field splitting can reduce the band gap energy both by introducing new occupied t_{2g} states above the e_g states of the original transition metal and by lowering its unoccupied t_{2g} states.

these calculations relating to $A^5 Al_2 O_4$ suggest that the oxidation states remain as 2+ throughout.

An increasing number of high-entropy transition metal oxides are active catalysts for the OER in alkaline conditions, including La(Cr,Mn,Fe,2Co,Ni)O $_3$, 22 (Co,Cu,Fe,Mn,Ni) $_3O_4$, 51 and AlNiCoRuMo oxide nanowires. 16 Given the possible synergistic effects of the five transition metals (including OER-active Fe $^{2+}$, Ni $^{2+}$, and Co $^{2+}$), along with the presence of Al $^{3+}$ that is known to have a promotional role that can improve catalytic activity 28,29 and the narrowed band gap that is expected to improve charge carrier transport, we sought to evaluate the OER activity of the high-entropy 5 Al $_2O_4$ spinel and compare it to each of the end members.

Linear sweep voltammetry revealed that only the highentropy $A^5 Al_2 O_4$ spinel, along with the $CoAl_2 O_4$ and $NiAl_2 O_4$ end members, generated a catalytic current above that of the glassy carbon substrate in the OER-relevant potential range of 1.2 to 1.9 V vs RHE; $FeAl_2 O_4$, $CuAl_2 O_4$, and $ZnAl_2 O_4$ were inactive (Figures 6a, S18, and S19). The high-entropy $A^5 Al_2 O_4$

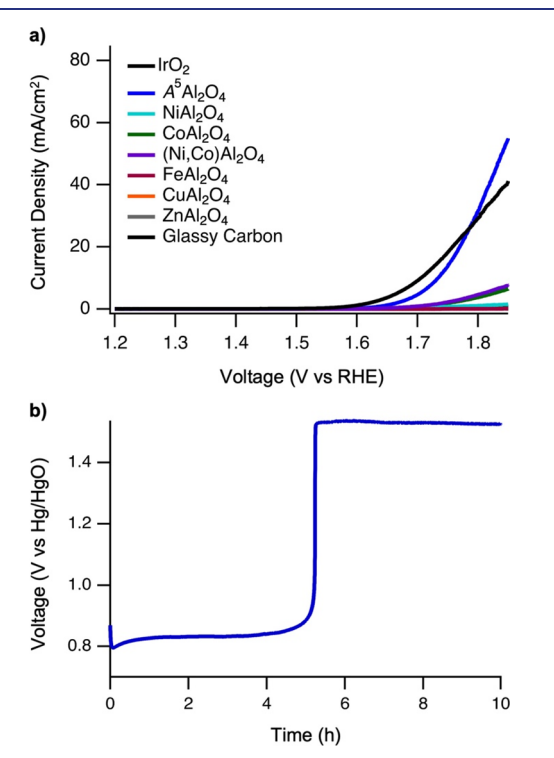


Figure 6. (a) Linear sweep voltammetry data for the OER in 1.0 M KOH for the AAl_2O_4 end members, $(Co,Ni)Al_2O_4$ solid solution, high-entropy $A^5Al_2O_4$ spinel, and a IrO_2 benchmark catalyst. Current is normalized to the electrochemically active surface area. (b) Chronopotentiometry data for the high-entropy $A^5Al_2O_4$ spinel, held at a constant current density of 10 mA/cm^2 .

spinel also outperformed $CoAl_2O_4$ and $NiAl_2O_4$ (Figure 6), as well as $(Co,Ni)Al_2O_4$ (Figure S20), a solid solution aluminate spinel that contains the two metals that are found to be active among the end members. $A^5Al_2O_4$ is therefore the highest-activity catalyst (based on overpotential required to achieve a current density of 10 mA/cm^2) among those tested. When normalized to the electrochemically active surface area (Figures 6a and S18), the high-entropy $A^5Al_2O_4$ spinel, which has a lower electrochemical surface area due to larger particle size, is comparatively more active than all of the parent compounds, as well as a bulk IrO_2 benchmark, at a potential of

1.7 V vs RHE. A⁵Al₂O₄ reached a current density of 10 mA/ cm² at an overpotential of 430 mV, whereas the IrO₂ catalyst reached this current density at an overpotential of 490 mV. Similar trends are observed when normalized to the geometric surface area (Figure S18a). The activity of the high-entropy A⁵Al₂O₄ spinel, which contains elements that are considered to be inexpensive and earth-abundant, is competitive with IrO₂, which is an expensive precious metal compound that is a benchmark catalyst for the OER. Based on the data in Figure 6a, the high-entropy $A^5Al_2O_4$ spinel is clearly an active catalyst on par with, or superior to, comparable existing materials. We suspect that both synergistic effects arising from the mixed metal surface, which offer complex active sites for the OER, and the band gap narrowing, which should significantly decrease resistance to the transport of carriers during electrocatalysis, is responsible for this enhanced performance.

While the surface is most likely dynamic and complex, the transport of carriers to this surface through the bulk of the catalyst material is still important for maximizing catalytic performance. Therefore, higher conductivity due to the narrowed band gap is advantageous to catalysis. To confirm that the narrowed band gap in $A^{\rm S}Al_2O_4$ correlates with increased conductivity and enhanced catalysis, we compared the admittance, which is a measure of conductivity, of $A^{\rm S}Al_2O_4$ to the most active parent phase, ${\rm CoAl_2O_4}$ (Figure S22). As expected from the narrowed band gap, we indeed observe an increase in conductivity in $A^{\rm S}Al_2O_4$.

In addition to activity, we also analyzed the stability of the high-entropy $A^5Al_2O_4$ spinel using chronopotentiometry, wherein the electrode is held at a constant current and potential is monitored over time, with a steady potential indicating stable catalytic performance. The data in Figure 6b shows that the high-entropy $A^5Al_2O_4$ spinel maintains nearly constant potential for approximately 5 h when held at a current density of 10 mA/cm^2 but then undergoes a sudden increase in voltage that is indicative of instability. Such instability could arise from catastrophic leaching, i.e., oxidative instability; decomposition, i.e., transformation into the constituent metal oxides or related compounds; or formation of a passivating layer, i.e., a catalytically inactive film that blocks the catalytically active surface.

Utilizing ICP-MS for the analysis of electrolyte aliquots during electrocatalysis, we do not observe dissolution of the high-entropy $A^5\mathrm{Al_2O_4}$ spinel (Figure S18b). The six metal analytes (Al, Fe, Co, Ni, Cu, Zn) remain at background partsper-billion levels; fluctuations at various time points remain within instrumental error and are not indicative of a measurable increase in solvated metals from potential catalyst dissolution. The ICP-MS data therefore rules out oxidative instability and leaching at the potentials applied during normal catalytic operation and confirms that the observed current is due to the OER and not corrosion.

Postcatalytic PXRD revealed that the high-entropy $A^5Al_2O_4$ spinel phase was still present (Figure S17c) as the bulk sample, although we cannot rule out the possibility that a small amount of one or more secondary phases may be present due to the small sample size. To better understand the catalytically relevant surface of the high-entropy $A^5Al_2O_4$ spinel, we aged a drop-cast layer of the $A^5Al_2O_4$ powder on a gold substrate, a technique previously employed to confirm the active phase of double-layered metal hydroxides. Utilizing GIXRD on the film, we find that a passivating layer of $K_{17}Fe_5O_{16}$ and K_2CoO_2 forms (Figure S18c). XRD peak matching (Figure S18c) was

used to attribute these potassium-containing phases to the passivating layer, although it is possible that they contain two or more metals. The incorporation of potassium on the surface was further confirmed by XPS (Figure S22). Neither K₁₇Fe₅O₁₆ nor K₂CoO₂ is a known OER catalyst, and the emergence of these phases correlates with inactivation of the catalyst. We therefore assume that they are catalytically inactive. In the future, it may be possible to suppress inactivation by preventing or minimizing formation of the passivating layer, perhaps through optimizing the mixing ratios of the 3d transition metals in A5Al2O4 or modifying the electrolyte. Taken together, these results suggest that the highentropy A⁵Al₂O₄ spinel fails after 5 h because of formation of a catalytically inactive passivating layer, not because of dissolution or decomposition. This, in turn, suggests that the HEO is likely to be the active catalyst.

CONCLUSIONS

The electronic changes in HEOs, compared to their end members, are not well understood, even though it is clear that complex solid solutions give rise to properties that are not an average of the properties of the end members. Here, we found that the high-entropy $A^5Al_2O_4$ spinel oxide, where A = Fe, Co, Ni, Cu, or Zn, has a band gap of 0.9 eV, which is narrower than the band gaps of all parent phases. Based on DFT calculations, this surprising property is theoretically shown to arise from the rearrangement of the electronic bands due to the energy shift of the 3d eg and tgg orbital states over broader energy ranges in the high-entropy spinel and the reduction of the crystal field splitting due to significant fractions of Cu and Zn. These insights provide guidelines for tuning the band gaps of HEO materials. The narrowed band gap in the high-entropy A⁵Al₂O₄ spinel is also advantageous for catalysis as its activity for the OER is enhanced relative to its end members.

ASSOCIATED CONTENT

Supporting Information

The Supporting Information is available free of charge at https://pubs.acs.org/doi/10.1021/jacs.2c12887.

Additional XRD, SEM-EDX, XPS, electrochemistry, and conductivity data; band structure calculations; Rietveld refinement data; and elemental analysis data (PDF)

AUTHOR INFORMATION

Corresponding Authors

Ismaila Dabo — Department of Materials Science and Engineering, The Pennsylvania State University, University Park, Pennsylvania 16802, United States; ⊚ orcid.org/0000-0003-0742-030X; Email: ixd4@psu.edu

Zhiqiang Mao – Department of Chemistry and Department of Physics, The Pennsylvania State University, University Park, Pennsylvania 16802, United States; Email: zim1@psu.edu

Raymond E. Schaak — Department of Chemistry, Department of Chemical Engineering, and Materials Research Institute, The Pennsylvania State University, University Park, Pennsylvania 16802, United States; Occid.org/0000-0002-7468-8181; Email: res20@psu.edu

Authors

Rowan R. Katzbaer – Department of Chemistry, The Pennsylvania State University, University Park, Pennsylvania 16802, United States

Francisco Marques dos Santos Vieira — Department of Materials Science and Engineering, The Pennsylvania State University, University Park, Pennsylvania 16802, United States

Complete contact information is available at: https://pubs.acs.org/10.1021/jacs.2c12887

Notes

The authors declare no competing financial interest.

ACKNOWLEDGMENTS

This work was supported by the National Science Foundation through the Penn State Materials Research Science and Engineering Center (MRSEC) DMR 2011839, as well as additional funds provided by Penn State University. TEM, SEM, XRD, XPS, and electrical data were acquired at the Materials Characterization Lab of the Penn State Materials Research Institute. ICP-MS data were acquired at the Laboratory for Isotopes and Metals in the Environment (LIME) at the Pennsylvania State University. The authors thank Lujin Min and Evan Krysko for helpful conversations on high-entropy spinels, Jeff Schallenberger for help with XPS analysis, Amira Meddeb for help with electrical properties measurements and analysis, and Maggie Wang for help with ICP-MS analysis.

REFERENCES

- (1) Sarkar, A.; Kruk, R.; Hahn, H. Magnetic Properties of High Entropy Oxides. *Dalton Trans.* **2021**, *50*, 1973–1982.
- (2) Witte, R.; Sarkar, A.; Kruk, R.; Eggert, B.; Brand, R. A.; Wende, H.; Hahn, H. H High-Entropy Oxides: An Emerging Prospect for Magnetic Rare-Earth Transition Metal Perovskites. *Phys. Rev. Mater.* **2019**, *3*, No. 034406.
- (3) Sarkar, A.; Wang, Q.; Schiele, A.; Chellali, M. R.; Bhattacharya, S. S.; Wang, D.; Brezesinski, T.; Hahn, H.; Velasco, L.; Breitung, B. High-Entropy Oxides: Fundamental Aspects and Electrochemical Properties. *Adv. Mater.* **2019**, *31*, No. 1806236.
- (4) Braun, J. L.; Rost, C. M.; Lim, M.; Giri, A.; Olson, D. H.; Kotsonis, G. N.; Stan, G.; Brenner, D. W.; Maria, J. P.; Hopkins, P. E. Charge-Induced Disorder Controls the Thermal Conductivity of Entropy-Stabilized Oxides. *Adv. Mater.* **2018**, *30*, No. 1805004.
- (5) Zhang, Y.; Lu, T.; Ye, Y.; Dai, W.; Zhu, Y.; Pan, Y. Stabilizing Oxygen Vacancy in Entropy-Engineered CoFe₂O₄-Type Catalysts for Co-Prosperity of Efficiency and Stability in an Oxygen Evolution Reaction. ACS Appl. Mater. Interfaces 2020, 12, 32548–32555.
- (6) Sun, Y.; Dai, S. High-Entropy Materials for Catalysis: A New Frontier. Sci. Adv. 2021, 7, 6589.
- (7) Chen, H.; Fu, J.; Zhang, P.; Peng, H.; Abney, C. W.; Jie, K.; Liu, X.; Chi, M.; Dai, S. Entropy-Stabilized Metal Oxide Solid Solutions as CO Oxidation Catalysts with High-Temperature Stability. *J. Mater. Chem. A* **2018**, *6*, 11129–11133.
- (8) Wu, D.; Kusada, K.; Nanba, Y.; Koyama, M.; Yamamoto, T.; Toriyama, T.; Matsumura, S.; Seo, O.; Gueye, I.; Kim, J.; Singgapulig, R.; Sakata, O.; Kawaguchi, S.; Kubota, Y.; Kitagawa, H. Noble-Metal High-Entropy-Alloy Nanoparticles: Atomic-Level Insight into the Electronic Structure. *J. Am. Chem. Soc.* **2022**, *144*, 3365–3369.
- (9) Rost, C. M.; Sachet, E.; Borman, T.; Moballegh, A.; Dickey, E. C.; Hou, D.; Jones, J. L.; Curtarolo, S.; Maria, J. P. Entropy-Stabilized Oxides. *Nat. Commun.* **2015**, *6*, 8485.
- (10) Wachs, I. E.; Routray, K. Catalysis Science of Bulk Mixed Oxides. ACS Catal. 2012, 2, 1235–1246.

- (11) Sarkar, A.; Loho, C.; Velasco, L.; Thomas, T.; Bhattacharya, S. S.; Hahn, H.; Djenadic, R. Multicomponent Equiatomic Rare Earth Oxides with a Narrow Band Gap and Associated Praseodymium Multivalency. *Dalton Trans.* **2017**, *46*, 12167–12176.
- (12) Sarkar, A.; Eggert, B.; Velasco, L.; Mu, X.; Lill, J.; Ollefs, K.; Bhattacharya, S. S.; Wende, H.; Kruk, R.; Brand, R. A.; Hahnm, H. Role of Intermediate 4f States in Tuning the Band Structure of High Entropy Oxides. *APL Mater.* **2020**, *8*, No. 05111.
- (13) Bérardan, D.; Franger, S.; Dragoe, D.; Meena, A. K.; Dragoe, N. Colossal Dielectric Constant in High Entropy Oxides. *Phys. Status Solidi RRL* **2016**, *10*, 328–333.
- (14) Rák, Z.; Maria, J. P.; Brenner, D. W. Evidence for Jahn-Teller Compression in the (Mg Co Ni Cu Zn)O Entropy-Stabilized Oxide: A DFT Study. *Mater. Lett.* **2018**, *217*, 300–303.
- (15) Sharma, Y.; Mazza, A. R.; Musico, B. L.; Skoropata, E.; Nepal, R.; Jin, R.; Ievlev, A. V.; Collins, L.; Gai, Z.; Chen, A.; et al. Magnetic Texture in Insulating Single Crystal High Entropy Oxide Spinel Films. *ACS Appl. Mater. Interfaces* **2021**, *13*, 17971–17977.
- (16) Jin, Z.; Lyu, J.; Zhao, Y. L.; Li, H.; Lin, X.; Xie, G.; Liu, X.; Kai, J. J.; Qiu, H. J. Rugged High-Entropy Alloy Nanowires with in Situ Formed Surface Spinel Oxide As Highly Stable Electrocatalyst in Zn-Air Batteries. ACS Mater. Lett. 2020, 2, 1698–1706.
- (17) Witte, R.; Sarkar, A.; Velasco, L.; Kruk, R.; Brand, R. A.; Eggert, B.; Ollefs, K.; Weschke, E.; Wende, H.; Hahn, H. Magnetic Properties of Rare-Earth and Transition Metal Based Perovskite Type High Entropy Oxides. *J. Appl. Phys.* **2020**, *127*, 185109.
- (18) Zhang, J.; Yan, J.; Calder, S.; Zheng, Q.; McGuire, M. A.; Abernathy, D. L.; Ren, Y.; Lapidus, S. H.; Page, K.; Zheng, H.; Freeland, J. W.; Budai, J.; Hermann, R. Long-Range Antiferromagnetic Order in a Rocksalt High Entropy Oxide. *Chem. Mater.* **2019**, *31*, 3705–3711.
- (19) Min, L.; Sretenovic, M.; Heitmann, T. W.; Valentine, T. W.; Zu, R.; Golpalan, V.; Rost, C. M.; Ke, X.; Mao, Z. A Topological Kagome Magnet in High Entropy Form. *Commun. Phys.* **2022**, *5*, 63.
- (20) Musicó, B.; Wright, Q.; Ward, T. Z.; Grutter, A.; Arenholz, E.; Gilbert, D.; Mandrus, D.; Keppens, V. Tunable Magnetic Ordering through Cation Selection in Entropic Spinel Oxides. *Phys. Rev. Mater.* **2019**, *3*, No. 104416.
- (21) Han, M.; Wang, Z.; Xu, Y.; Wu, R.; Jiao, S.; Chen, Y.; Feng, S. Physical Properties of MgAl₂O₄, CoAl₂O₄, NiAl₂O₄, CuAl₂O₄, and ZnAl₂O₄ Spinels Synthesized by a Solution Combustion Method. *Mater. Chem. Phys.* **2018**, 215, 251–258.
- (22) Nguyen, T. X.; Liao, Y. C.; Lin, C. C.; Su, Y. H.; Ting, J. M. Advanced High Entropy Perovskite Oxide Electrocatalyst for Oxygen Evolution Reaction. *Adv. Funct. Mater.* **2021**, *31*, No. 2101632.
- (23) Mao, A.; Xiang, H. Z.; Zhang, Z. G.; Kuramoto, K.; Zhang, H.; Jia, Y. A New Class of Spinel High-Entropy Oxides with Controllable Magnetic Properties. *J. Magn. Magn. Mater.* **2020**, 497, 165884.
- (24) Dąbrowa, J.; Stygar, M.; Mikuła, A.; Knapik, A.; Mroczka, K.; Tejchman, W.; Danielewski, M.; Martin, M. Synthesis and Microstructure of the (Co,Cr,Fe,Mn,Ni)₃O₄ High Entropy Oxide Characterized by Spinel Structure. *Mater. Lett.* **2018**, 216, 32–36.
- (25) Yang, Y.; Peltier, C. R.; Zeng, R.; Schimmenti, R.; Li, Q.; Huang, X.; Yan, Z.; Potsi, G.; Selhorst, R.; Lu, X.; Xu, W.; Tader, M.; Soudackov, A.; Zhang, H.; Krumov, M.; Murray, E.; Xu, P.; Hitt, J.; Xu, L.; Ko, H.; Ernst, B.; Bundschu, C.; Luo, A.; Markovichm, D.; Hu, M.; He, C.; Wang, H.; Fang, J.; DiStasio, R. A.; Kourkoutis, L. F.; Singer, A.; Noonan, K. J. T.; Xiao, L.; Zhuang, L.; Pivovar, B. S.; Zelenay, P.; Herrero, E.; Feliu, J. M.; Suntivich, J.; Giannelis, E. P. Electrocatalysis in Alkaline Media and Alkaline Membrane-Based Energy Technologies. *Chem. Rev.* 2022, 122, 6117–6321.
- (26) Roy Chowdhury, S.; Ray, A.; Chougule, S. S.; Min, J.; Jeffery, A. A.; Ko, K.; Kim, Y.; Das, S.; Jung, N. Mixed Spinel Ni–Co Oxides: An Efficient Bifunctional Oxygen Electrocatalyst for Sustainable Energy Application. ACS Appl. Energy Mater. 2022, 5, 4421–4430.
- (27) Menezes, P. W.; Indra, A.; Sahraie, N. R.; Bergmann, A.; Strasser, P.; Driess, M. Cobalt-Manganese-Based Spinels as Multifunctional Materials That Unify Catalytic Water Oxidation and Oxygen Reduction Reactions. *ChemSusChem* **2015**, *8*, 164–171.

- (28) Gerken, J. B.; Chen, J. Y. C.; Massé, R. C.; Powell, A. B.; Stahl, S. S. Development of an O₂-Sensitive Fluorescence-Quenching Assay for the Combinatorial Discovery of Electrocatalysts for Water Oxidation. *Angew. Chem., Int. Ed.* **2012**, *51*, 6676–6680.
- (29) Chen, J. Y. C.; Miller, J. T.; Gerken, J. B.; Stahl, S. S. Inverse Spinel NiFeAlO₄ as a Highly Active Oxygen Evolution Electrocatalyst: Promotion of Activity by a Redox-Inert Metal Ion. *Energy Environ. Sci.* **2014**, *7*, 1382–1386.
- (30) Murphy, A. B. Band-Gap Determination from Diffuse Reflectance Measurements of Semiconductor Films, and Application to Photoelectrochemical Water-Splitting. *Sol. Energy Mater. Sol. Cells* **2007**, *91*, 1326–1337.
- (31) George, P.; Chowdhury, P. Complex Dielectric Transformation of UV-Vis Diffuse Reflectance Spectra for Estimating Optical Band-Gap Energies and Materials Classification. *Analyst* **2019**, *144*, 3005—3012.
- (32) Giannozzi, P.; Baroni, S.; Bonini, N.; Calandra, M.; Car, R.; Cavazzoni, C.; Ceresoli, D.; Chiarotti, G.; Cococcioni, M.; Dabo, I.; Dal Corso, A.; De Gironcoli, S.; Fabris, S.; Fratesi, G.; Gebauer, R.; Gerstmann, U.; Gougoussis, C.; Kokalj, A.; Lazzeri, M.; Martin-Samos, L.; Marzari, N.; Mauri, F.; Mazzarello, R.; Paolini, S.; Pasquarello, A.; Paulatto, L.; Sbraccia, C.; Scandolo, S.; Sclauzero, G.; Seitsonen, A.; Smogunov, A.; Umari, P.; Wentzcovitch, R. Quantum ESPRESSO: A modular and open-source software project for quantum simulations of materials. *J. Phys.: Condens. Matter* 2009, 21, No. 395502.
- (33) Giannozzi, P.; Andreussi, O.; Brumme, T.; Bunau, O.; Buongiorno Nardelli, M.; Calandra, M.; Car, R.; Cavazzoni, C.; Ceresoli, D.; Cococcioni, M.; Colonna, N.; Carnimeo, I.; Dal Corso, A.; de Gironcoli, S.; Delugas, P.; DiStasio, R. A., Jr.; Ferretti, A.; Floris, A.; Fratesi, G.; Fugallo, G.; Gebauer, R.; Gerstmann, U.; Giustino, F.; Gorni, T.; Jia, J.; Kawamura, M.; Ko, H. Y.; Kokalj, A.; Küçükbenli, E.; Lazzeri, M.; Marsili, M.; Marzari, N.; Mauri, F.; Nguyen, N. L.; Nguyen, H. V.; Otero-de-la Rosa, A.; Paulatto, L.; Poncé, S.; Rocca, D.; Sabatini, R.; Santra, B.; Schlipf, M.; Seitsonen, A.; Smogunov, A.; Timrov, I.; Thonhauser, T.; Umari, P.; Vast, N.; Baroni, S. Advanced capabilities for materials modelling with Quantum ESPRESSO. J. Phys.: Condens. Matter 2017, 29, 465901.
- (34) Giannozzi, P.; Baseggio, O.; Bonfa, P.; Brunato, D.; Car, R.; Carnimeo, I.; Cavazzoni, C.; de Gironcoli, S.; Delugas, P.; Ferrari Ruffino, F.; Ferretti, A.; Marzari, N.; Timrov, I.; Urru, A.; Baroni, S. Quantum ESPRESSO toward the exascale. *J. Chem. Phys.* **2020**, *152*, 154105.
- (35) Perdew, J.; Burke, K.; Ernzerhof, M. Generalized gradient approximation made simple. *Phys. Rev. Lett.* **1996**, *77*, 3865.
- (36) SSSP; Prandini, G.; Marrazzo, A.; Castelli, I. E.; Mounet, N.; Marzari, N. npj Comput. Mater. 2018, 4, 72.
- (37) Lejaeghere, K.; Bihlmayer, G.; Björkman, T.; Blaha, P.; Blügel, S.; Blum, V.; Caliste, D.; Castelli, I. E.; Clark, S. J.; Corso, A. D.; de Gironcoli, S.; Deutsch, T.; Dewhurst, J. K.; Marco, I. D.; Draxl, C.; Dułak, M.; Eriksson, O.; Flores-Livas, J. A.; Garrity, K. F.; Genovese, L.; Giannozzi, P.; Giantomassi, M.; Goedecker, S.; Gonze, X.; Grånäs, O.; Gross, E. K. U.; Gulans, A.; Gygi, F.; Hamann, D. R.; Hasnip, P. J.; Holzwarth, N. A. W.; Iuşan, D.; Jochym, D. B.; Jollet, F.; Jones, D.; Kresse, G.; Koepernik, K.; Küçükbenli, E.; Kvashnin, Y. O.; Locht, I. L. M.; Lubeck, S.; Marsman, M.; Marzari, N.; Nitzsche, U.; Nordström, L.; Ozaki, T.; Paulatto, L.; Pickard, C. J.; Poelmans, W.; Probert, M. I. J.; Refson, K.; Richter, M.; Rignanese, G.; Saha, S.; Scheffler, M.; Schlipf, M.; Schwarz, K.; Sharma, S.; Tavazza, F.; Thunström, P.; Tkatchenko, A.; Torrent, M.; Vanderbilt, D.; van Setten, M. J.; Speybroeck, V.; Wills, J. M.; Yates, J. R.; Zhang, G.; Cottenier, S. Reproducableity in Density Functional Theory Calcuations of Solids. Science 2016, 351, 3000.
- (38) Anisimov, V.; Zaanen, J.; Andersen, O. Band theory and Mott insulators: Hubbard U instead of Stoner I. *Phys. Rev. B* **1991**, *44*, 943. (39) Anisimov, V.; Aryasetiawan, F.; Liechtenstein, A. First-principles calculations of the electronic structure and spectra of strongly correlated systems: the LDA+U method. *J. Phys.: Condens. Matter* **1997**, *9*, 767.

- (40) Dudarev, S.; Botton, G.; Savrasov, S.; Humphreys, C.; Sutton, A. Electron-energy-loss spectra and the structural stability of nickel oxide: An LSDA+U study. *Phys. Rev. B* **1998**, *57*, 1505.
- (41) Löwdin, P. O. On the non-orthogonality problem connected with the use of atomic wave functions in the theory of molecules and crystals. *J. Chem. Phys.* **1950**, *18*, 365.
- (42) Pathak, N.; Gupta, S. K.; Sanyal, K.; Kumar, M.; Kadam, R. M.; Natarajan, V. Photoluminescence and EPR Studies on Fe³⁺ Doped ZnAl₂O₄: An Evidence for Local Site Swapping of Fe³⁺ and Formation of Inverse and Normal Phase. *Dalton Trans.* **2014**, *43*, 9319–9323.
- (43) Jastrzębska, I.; Szczerba, J.; Błachowski, A.; Stoch, P. Structure and Microstructure Evolution of Hercynite Spinel (Fe²⁺Al₂O₄) after Annealing Treatment. *Eur. J. Mineral.* **2017**, *29*, 62–71.
- (44) Popescu, M.; Ghizdeanu, C. Cation Distribution in Cobalt Ferrite-Aluminates. In *Phys. Stat. Sol. A*; De Gruyter, 1979, Vol. 52; pp 785–788.
- (45) De, K. S.; Ghose, J.; Murthy, K. S. R. C. Solid State Sudies on Substituted CuCr₂O₄. *J. Solid State Chem.* **1983**, 47, 264–277.
- (46) Walsh, A.; Wei, S. H.; Yan, Y.; Al-Jassim, M. M.; Turner, J. A.; Woodhouse, M.; Parkinson, B. A. Structural, Magnetic, and Electronic Properties of the Co-Fe-Al Oxide Spinel System: Density-Functional Theory Calculations. *Phys. Rev. B: Condens. Matter Mater. Phys.* **2007**, 76, No. 165119.
- (47) Yao, T.; Imafuji, O.; Jinno, H. EXAFS Study of Cation Distribution in Nickel Aluminate Ferrites. J. Am. Ceram. Soc. 1991, 74, 314–317
- (48) Biesinger, M.; Lau, L.; Gerson, A.; Smart, R. Resolving surface chemical states in XPS analysis of first row transition metals, oxides and hydroxides: Sc, Ti V, Cu and Zn. *Appl. Surf. Sci.* **2010**, 257, 887–898.
- (49) Biesinger, M.; Payne, B.; Grosvenor, A.; Lau, L.; Gerson, A.; Smart, R. Resolving surface chemical states in XPS analysis of first row transition metals, oxides, and hydroxides: Cr, Mn, Fe, Co, and Ni. *Appl. Surf. Sci.* **2011**, *257*, *2717*–*2730*.
- (50) Li, L.; Gan, Y. M.; Lu, Z. H.; Yu, X.; Qing, S.; Gao, Z.; Zhang, R.; Feng, G. The Effects of Fe, Co and Ni Doping in CuAl₂O₄ Spinel Surface and Bulk: A DFT Study. *Appl. Surf. Sci.* **2020**, *521*, No. 146478.
- (51) Wang, D.; Liu, Z.; Du, S.; Zhang, Y.; Li, H.; Xiao, Z.; Chen, W.; Chen, R.; Wang, Y.; Zou, Y.; Wang, S. Low-Temperature Synthesis of Small-Sized High-Entropy Oxides for Water Oxidation. *J. Mater. Chem. A* 2019, 7, 24211–24216.
- (52) Trotochaud, L.; Young, S. L.; Ranney, J. K.; Boettcher, S. W. Nickel-Iron Oxyhydroxide Oxygen-Evolution Electrocatalysts: The Role of Intentional and Incidental Iron Incorporation. *J. Am. Chem. Soc.* **2014**, *136*, 6744–6753.

Recommended by ACS

Hybrid Functional-Based Scissors Operator for Perovskite Oxide Nanostructures: A NaTaO₃ Case Study

Guilherme Ribeiro Portugal and Jeverson Teodoro Arantes

MARCH 09, 2023

THE JOURNAL OF PHYSICAL CHEMISTRY C

READ 🗹

Insights into the Use of Te-O Pairs as Active Centers of Carbon Nanosheets for Efficient Electrochemical Oxygen Reduction

Zeming Wang, Minghong Wu, et al.

APRIL 17, 2023

ACS NANO

READ 🗹

Fast Surface Oxygen Release Kinetics Accelerate Nanoparticle Exsolution in Perovskite Oxides

Jiayue Wang, Bilge Yildiz, et al.

JANUARY 10, 2023

JOURNAL OF THE AMERICAN CHEMICAL SOCIETY

RFAD **[**✓

Doping Shortens the Metal/Metal Distance and Promotes OH Coverage in Non-Noble Acidic Oxygen Evolution Reaction Catalysts

Ning Wang, Edward H. Sargent, et al.

APRIL 03, 2023

JOURNAL OF THE AMERICAN CHEMICAL SOCIETY

READ 🗹

Get More Suggestions >